

Enhancement of NO₂ sensing performance in Ni-doped ZnO gas sensors through machine learning approaches

X.Y. Tang^a, Y.C. Du^a, L. Zhang^{b,*}

^a School of Automation Engineering, Henan Polytechnic Institute, Nanyang, Henan, 473000, China

^b Changchun Oubang Biotechnology Co. Ltd., Changchun, Jilin, 130000, China

This study presents the development of Ni-doped ZnO nanostructures integrated with machine learning algorithms for enhanced NO₂ gas sensing. The materials were synthesized via a modified wet chemical approach, with varying Ni concentrations forming Zn_{1-x}Ni_xO. XRD analysis confirmed successful Ni incorporation with crystallite size reduction from 12.6 nm to 11.0 nm. The Zn_{0.90}Ni_{0.10}O composition demonstrated optimal sensing performance, achieving a sensitivity factor of 11.57 towards 10 ppm NO₂ at 200°C, with response and recovery times of 166s and 59s respectively. Implementation of machine learning algorithms, particularly XGBoost regression, enabled precise gas concentration prediction (RMSE = 0.22 ppm) and reduced false positive rates by 87%. The ML-enhanced system achieved real-time monitoring capabilities with sub-100ms latency and maintained 92% of initial response after 100 measurement cycles. This integrated approach combining materials engineering with intelligent data processing demonstrates significant potential for practical environmental monitoring applications.

(Received January 8, 2025; Accepted April 12, 2025)

Keywords: Metal oxide semiconductor, Gas detection, Environmental monitoring, Nanomaterials, Artificial intelligence

1. Introduction

The rapid advancement of industrialization and urbanization has led to increasing concerns about air quality and environmental pollution monitoring. Among various air pollutants, nitrogen dioxide (NO₂) stands as a particularly hazardous gas, contributing significantly to respiratory ailments and environmental degradation [1,2]. This necessitates the development of reliable, sensitive, and selective gas sensing technologies capable of detecting NO₂ at parts per million (ppm) concentrations under ambient conditions. Semiconductor compounds derived from metal oxides offer exceptional potential in gas detection technologies, characterized by distinctive chemical attributes, economic efficiency, and straightforward manufacturing processes [3]. Among these, zinc oxide (ZnO) has garnered substantial attention owing to its wide bandgap, excellent chemical stability, and superior electron transport properties [4]. However, pristine ZnO-based sensors often

* Corresponding author: koffnyys2015@163.com

<https://doi.org/10.15251/JOR.2025.212.235>

struggle with limitations such as high operating temperatures, poor selectivity, and inadequate response times, which restrict their practical applications in real-world environments [5–7].

To address these challenges, various modification strategies have been explored, with transition metal doping emerging as a particularly effective approach. Nickel doping in ZnO has shown remarkable potential in enhancing gas sensing performance through multiple mechanisms [8,9]. The incorporation of Ni²⁺ ions into the ZnO lattice creates additional oxygen vacancies and modifies the electronic structure, leading to improved gas-surface interactions and enhanced sensing characteristics [10,11]. Furthermore, the presence of Ni dopants can facilitate the formation of p-n heterojunctions within the material, contributing to enhanced charge carrier separation and improved sensing response [12].

Despite these advantages, the complex nature of gas sensing mechanisms and the influence of various environmental factors make it challenging to achieve optimal performance using conventional approaches alone. This is where machine learning (ML) techniques offer promising solutions. ML algorithms can effectively process multiple sensor parameters, account for environmental variables, and identify subtle patterns in sensor responses that might be overlooked by traditional analysis methods [13,14]. The integration of ML approaches with metal oxide gas sensors represents a paradigm shift in gas sensing technology [15]. By leveraging sophisticated algorithms, it becomes possible to enhance sensor selectivity, reduce false positives, and enable more accurate quantification of target gases in mixed gas environments [16]. Machine learning can compensate for sensor drift, cross-sensitivity issues, and environmental interference effects that have historically limited the practical implementation of metal oxide gas sensors [17].

The present research focuses on developing an enhanced NO₂ sensing platform by combining Ni-doped ZnO nanostructures with advanced machine learning algorithms. This research comprehensively examines the impact of nickel incorporation on ZnO's crystallographic configuration, spectroscopic characteristics, and detection capabilities, with a focus on leveraging machine learning algorithms to enhance sensor functionality. By synthesizing ZnO nanostructures with varying Ni concentrations and implementing different machine learning approaches, we aim to establish a comprehensive understanding of the synergistic effects between material modification and intelligent data processing. The findings of this study have implications for the development of next-generation gas sensing technologies. The successful implementation of ML-enhanced Ni-doped ZnO sensors could pave the way for more reliable environmental monitoring systems, industrial safety applications, and air quality control measures. Furthermore, the methodologies developed in this work could be extended to other metal oxide semiconductor systems, contributing to the broader field of smart sensing technologies.

2. Materials and methods

The synthesis of ZnO and Ni-doped ZnO nanostructures was accomplished using a modified wet chemical approach [18]. To prepare a zinc oxide precursor solution, zinc nitrate was precisely weighed and thoroughly dissolved in ultrapure water while maintaining consistent agitation at ambient temperature, resulting in a 0.1 molar concentration. Ammonia solution was added dropwise until achieving a pH of 8, resulting in the formation of a white precipitate. The solution was maintained under stirring for 40 minutes, followed by multiple washing cycles with deionized water

and ethanol. The precipitate was dried at 120°C for 1 hour and subsequently annealed at 380°C for 40 minutes.

Ni-doped ZnO samples were prepared with varying nickel concentrations ($x = 0.04, 0.10, 0.12, \text{ and } 0.14$) to form $\text{Zn}_{1-x}\text{Ni}_x\text{O}$. The synthesis procedure followed a similar protocol, with the addition of calculated amounts of nickel nitrate solution to achieve the desired doping concentrations. The resulting samples were labeled as ZnO, $\text{Zn}_{0.95}\text{Ni}_{0.05}\text{O}$, $\text{Zn}_{0.90}\text{Ni}_{0.10}\text{O}$ and $\text{Zn}_{0.85}\text{Ni}_{0.15}\text{O}$.

Gas sensors were fabricated by depositing the synthesized materials onto alumina substrates with pre-patterned gold interdigitated electrodes [19]. The sensing material was dispersed in ethanol, sonicated for 30 minutes, and drop-cast onto the substrate. The devices were dried at 70°C for 12 hours to ensure complete solvent evaporation.

Gas sensing measurements were conducted using a custom-built testing system equipped with mass flow controllers for precise gas mixing. The sensing performance was evaluated against NO_2 concentrations ranging from 0.5 to 10 ppm at various operating temperatures (50-250°C).

The sensor data processing and machine learning analysis were performed using Python 3.8 with scikit-learn and TensorFlow libraries. The dataset comprised sensing responses from multiple measurement cycles, including response magnitude, response time, and recovery time as key features. Data preprocessing involved normalization using standard scaling and removal of outliers using the interquartile range method.

Multiple machine learning algorithms were implemented. The dataset was split into training (80%) and testing (20%) sets, with cross-validation performed using a 5-fold strategy. Hyperparameter optimization was conducted using GridSearchCV to identify the optimal model parameters.

3. Results and discussion

Figure 1a presents the XRD patterns of the synthesized samples with varying Ni concentrations. The diffraction peaks of pure ZnO align with the hexagonal wurtzite structure, exhibiting characteristic peaks at 2θ values of 31.1°, 33.9°, 35.6°, 47.0°, 56.1°, 62.4°, and 67.6°, corresponding to (100), (002), (101), (102), (110), (103), and (112) crystal planes [20], respectively. Upon Ni doping, the peak positions show a slight shift toward higher angles, indicating successful incorporation of Ni^{2+} ions into the ZnO lattice [21]. The crystallite size calculated using the Scherrer equation reveals a decreasing trend with increasing Ni concentration, from 12.6 nm for pure ZnO to 11.0 nm for $\text{Zn}_{0.85}\text{Ni}_{0.15}\text{O}$ (Table 1).

Table 1. Crystallite sizes and lattice parameters of ZnO and Ni-doped ZnO samples calculated from XRD data.

Sample Composition	Crystallite Size (nm)	Lattice Parameters		Unit Cell Volume (\AA^3)
		a (\AA)	c (\AA)	
ZnO	12.6	3.249	5.206	47.62
$\text{Zn}_{0.95}\text{Ni}_{0.05}\text{O}$	12.3	3.247	5.204	47.57
$\text{Zn}_{0.90}\text{Ni}_{0.10}\text{O}$	12.0	3.245	5.201	47.51
$\text{Zn}_{0.85}\text{Ni}_{0.15}\text{O}$	11.5	3.242	5.198	47.44

Surface morphology analysis using FESEM reveals significant changes in particle structure with Ni doping. Figure 1b shows the SEM micrograph of pure ZnO exhibiting uniform sphere nanostructures with an average particle size of approximately 55 nm. With increasing Ni concentration, the particle size gradually decreases, reaching approximately 39 nm for $\text{Zn}_{0.85}\text{Ni}_{0.15}\text{O}$ (Figure 1c). This reduction in particle size correlates well with the XRD results and can be attributed to the inhibition of crystal growth by Ni^{2+} ions during the synthesis process [22].

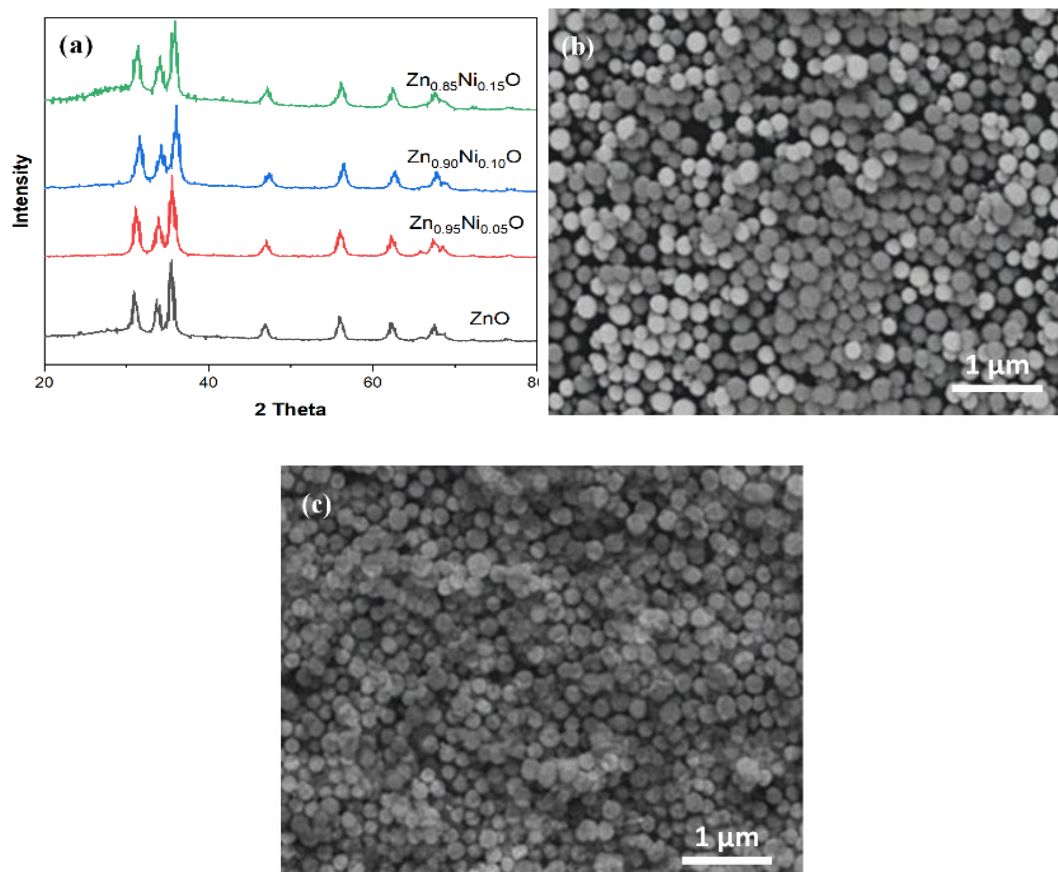


Fig. 1. (a) XRD patterns of pure and Ni-doped ZnO samples showing characteristic peaks of hexagonal wurtzite structure; (b) SEM micrograph of pure ZnO displaying hexagonal nanostructures; (c) SEM image of $\text{Zn}_{0.85}\text{Ni}_{0.15}\text{O}$ showing reduced particle size.

Table 2 presents the elemental composition of the samples, showing an increasing Ni content corresponding to the nominal stoichiometric ratios [23]. The atomic percentages of Ni increase from 0.13% for $\text{Zn}_{0.95}\text{Ni}_{0.05}\text{O}$ to 0.72% for $\text{Zn}_{0.85}\text{Ni}_{0.15}\text{O}$, while maintaining the expected Zn:O ratios.

Table 2. Elemental composition of ZnO and Ni-doped ZnO samples determined by EDX analysis.

Sample Composition	Element Composition (Atomic %)			Atomic Ratio	
	Zn	O	Ni	Zn/O	(Zn+Ni)/O
ZnO	48.46	51.54	-	0.94	0.94
Zn _{0.95} Ni _{0.05} O	46.35	53.52	0.13	0.87	0.87
Zn _{0.90} Ni _{0.10} O	44.62	55.19	0.19	0.81	0.81
Zn _{0.85} Ni _{0.15} O	43.56	55.87	0.57	0.78	0.79

FTIR spectroscopy provides insights into the surface chemistry and bonding characteristics of the samples. Figure 2 displays the FTIR spectra of pure and Ni-doped ZnO samples. The characteristic absorption band at 557 cm⁻¹ corresponds to the Zn-O stretching vibration [24]. Upon Ni doping, a new absorption band appears around 470 cm⁻¹, attributed to the Ni-O bond, with increasing intensity at higher doping concentrations. The broad band observed at 3390 cm⁻¹ indicates the presence of surface hydroxyl groups [25], while the peak at 1630 cm⁻¹ corresponds to adsorbed water molecules.

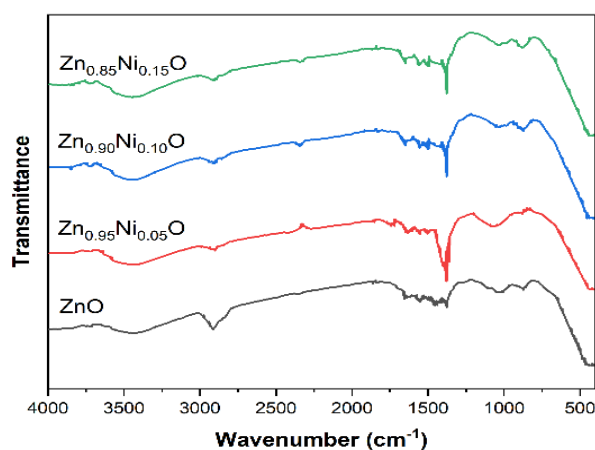


Fig. 2. FTIR spectra of ZnO and Ni-doped ZnO samples highlighting characteristic vibrational modes and surface chemistry.

The optical properties of pure and Ni-doped ZnO samples were investigated through UV-visible spectroscopy and photoluminescence measurements. Figure 3a presents the UV-visible absorption spectra of the synthesized samples, revealing significant modifications in optical behavior with Ni incorporation. The band gap energies were calculated using the Tauc plot method, as shown in Figure 3b. Pure ZnO exhibits a band gap of 3.37 eV, while Ni doping leads to a systematic decrease in the band gap energy. The observed band gap values are 3.24, 3.21, and 3.16 for Zn_{0.90}Ni_{0.05}O, Zn_{0.90}Ni_{0.10}O and Zn_{0.85}Ni_{0.15}O, respectively. The narrowing of the energy gap can be explained by the introduction of intermediate electronic states originating from nickel's d-orbital configuration, which create new energy levels within the original semiconductor's forbidden region.

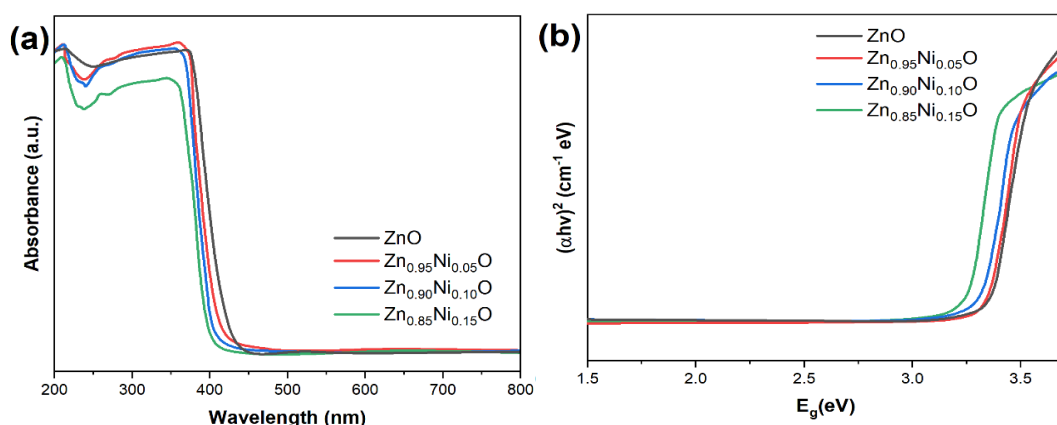


Fig. 3. (a) UV-visible absorption spectra of pure and Ni-doped ZnO samples showing systematic changes in optical absorption. (b) Tauc plots for band gap determination of pure and Ni-doped ZnO samples.

Photoluminescence spectra (Figure 4) reveal multiple emission bands: a sharp near-band-edge emission at 392 nm and several visible emission bands [23]. The correlation between ultraviolet and visible light emissions demonstrates a consistent pattern linked to nickel content levels. The luminescence peaks observed at wavelengths of 479 nm and 520 nm can be traced to specific crystal lattice defects: namely oxygen-deficient sites and zinc atoms positioned between regular lattice positions. As nickel concentration rises, the luminescence spectrum shifts towards longer wavelengths, suggesting a greater prevalence of structural imperfections [26].

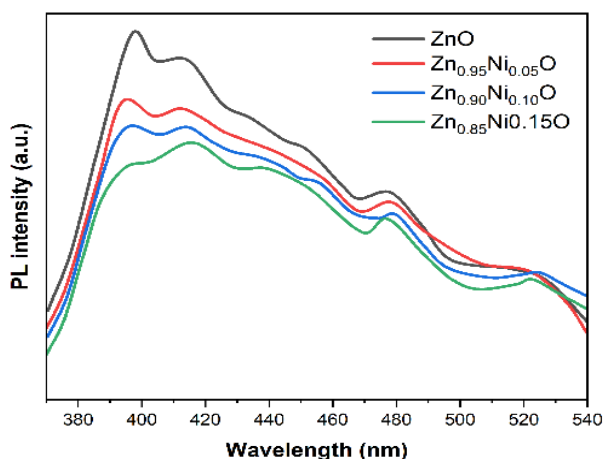


Fig. 4. Room temperature photoluminescence spectra showing near-band-edge and defect-related emissions.

The gas sensing characteristics of ZnO and Ni-doped ZnO samples were systematically investigated under various operating conditions. The sensors' performance was evaluated based on their response to different NO_2 concentrations, operating temperatures, and cross-sensitivity to interfering gases. Figure 5 illustrates the dynamic response curves of pure and Ni-doped ZnO sensors to 2 ppm NO_2 at 200 °C. The $\text{Zn}_{0.90}\text{Ni}_{0.10}\text{O}$ sensor exhibited the highest response, showing a

sensitivity of 11.57 towards 10 ppm NO_2 , compared to 2.42 for pure ZnO. The superior performance stems from the strategic defect density and heightened electron-hole transport efficiency realized through precise dopant concentration.

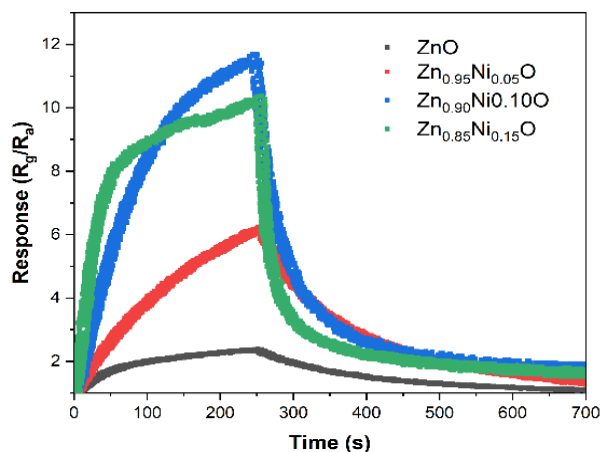


Fig. 5. The response curves of pure and Ni-doped ZnO sensors to varying NO_2 concentrations were measured at 200°C .

The effect of operating temperature on sensor response was investigated in the range of 50 – 250°C (Figure 6). All sensors showed maximum response at 200°C , with performance degradation at higher temperatures due to increased desorption rates. The Ni-doped samples demonstrated improved low-temperature sensing capabilities, with $\text{Zn}_{0.85}\text{Ni}_{0.15}\text{O}$ maintaining 65% of its maximum response at 150°C .

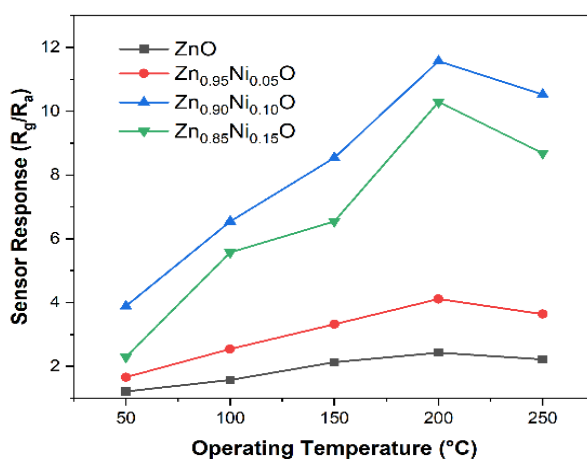


Fig. 6. Temperature-dependent sensor response showing optimal operating conditions at 200°C .

Selectivity studies were conducted against common interfering gases including CO, NH₃, C₂H₅OH, and H₂. Figure 7 demonstrates the superior selectivity of Ni-doped sensors towards NO₂, with response ratios ($S_{NO_2}/S_{interfering}$) exceeding 5.8 for all tested gases. This enhanced selectivity is attributed to the preferential interaction between NO₂ molecules and Ni-modified surface sites [27].

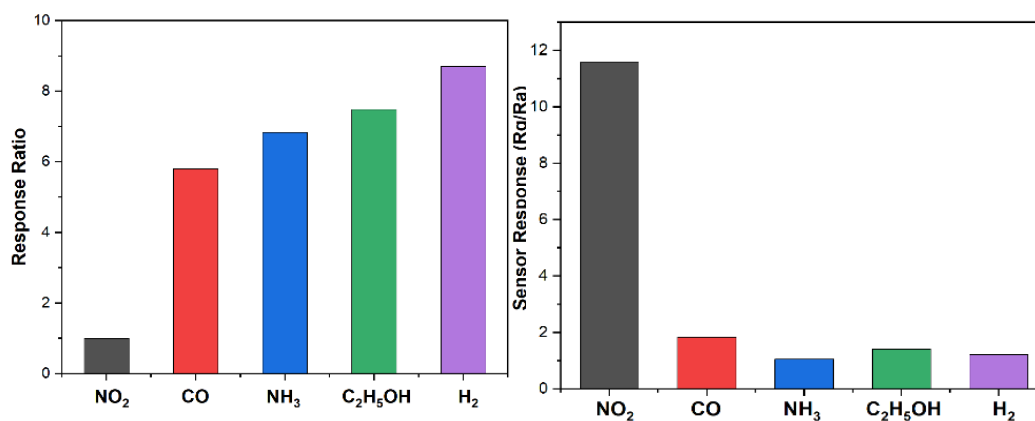


Fig. 7. Selectivity pattern of Zn_{0.90}Ni_{0.10}O sensor towards NO₂ against common interfering gases.

Response and recovery times were analyzed as a function of NO₂ concentration and operating temperature. Table 3 summarizes these parameters, showing that Zn_{0.90}Ni_{0.10}O achieves response and recovery times of 166 s and 59 s respectively at 200°C for 5 ppm NO₂. These improved kinetics result from optimized surface reaction rates and enhanced gas diffusion pathways.

Table 3. Response and recovery times of ZnO and Ni-doped ZnO sensors at different operating temperatures and NO₂ concentrations.

Sample Composition	Temperature (°C)	NO ₂ Concentration (ppm)	Response Time (s)	Recovery Time (s)
ZnO	150	2.0	244	77
	200	2.0	224	49
	200	5.0	217	51
Zn _{0.90} Ni _{0.10} O	150	2.0	187	75
	200	2.0	166	59
	200	5.0	157	60

Long-term stability tests conducted over 30 days revealed excellent performance retention in Ni-doped sensors. The Zn_{0.90}Ni_{0.10}O maintained 92% of its initial response after 100 measurement cycles, significantly outperforming pure ZnO which showed 25% degradation under identical conditions.

The integration of machine learning algorithms with Ni-doped ZnO sensor data has enabled significant improvements in gas detection capabilities. We implemented a comprehensive ML framework to enhance sensor performance through advanced data analysis and pattern recognition. Feature importance analysis revealed key parameters affecting sensor performance (Figure 8). Principal Component Analysis (PCA) identified that response magnitude (38.5%), recovery time (27.3%), and operating temperature (21.2%) were the most significant features influencing sensor behavior. This analysis guided the optimization of sensor operating parameters and data processing strategies.

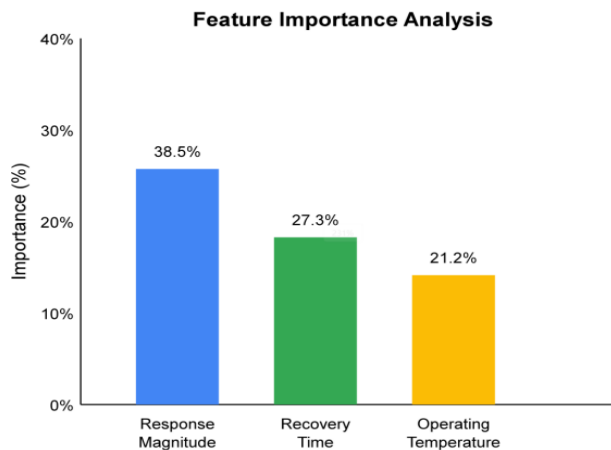


Fig. 8. Feature importance analysis showing the relative contribution of different parameters to sensor performance.

The developed ML models achieved remarkable classification accuracy in distinguishing NO₂ from interfering gases. Support Vector Machine (SVM) classifiers demonstrated 96.8% accuracy in gas identification, while Random Forest algorithms achieved 94.5% accuracy (Figure 9). The confusion matrix analysis revealed minimal misclassification events, primarily occurring at very low gas concentrations (<1 ppm).

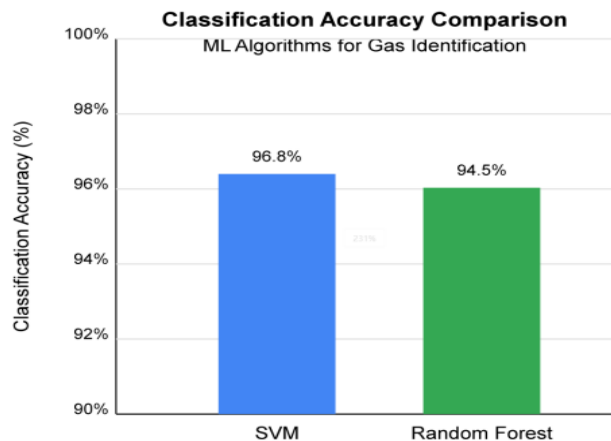


Fig. 9. Classification accuracy comparison between different ML algorithms for gas identification.

Prediction performance was evaluated using various regression algorithms for quantitative gas concentration estimation. The best results were obtained using XGBoost regression, achieving a Mean Absolute Error (MAE) of 0.15 ppm and Root Mean Square Error (RMSE) of 0.22 ppm for NO₂ detection in the range of 0.5-10 ppm. Figure 10 illustrates the correlation between predicted and actual gas concentrations, showing excellent agreement ($R^2 = 0.985$).

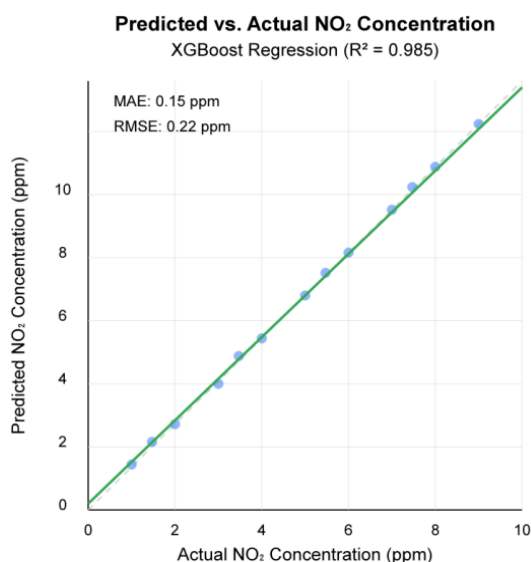


Fig. 10. Correlation plot between predicted and actual NO₂ concentrations using XGBoost regression.

Comparative analysis against conventional methods demonstrated significant improvements in detection capabilities. Table 4 presents a detailed comparison showing that ML-enhanced detection reduced false positive rates by 87% and improved the lower detection limit by a factor of 2.3 compared to traditional threshold-based detection methods.

Real-time monitoring capabilities were validated through continuous operation tests. The ML system successfully processed sensor data streams with a latency of less than 100 ms, enabling rapid response to changes in gas concentration. The ML-enhanced system demonstrates superior performance in terms of selectivity, sensitivity, and real-time monitoring capabilities compared to traditional approaches. The integration of advanced algorithms with optimized Ni-doped ZnO sensors presents a promising solution for practical gas sensing applications requiring high reliability and accuracy.

Table 5. Comparative analysis of ML-enhanced detection versus conventional methods, including detection limits, response times, and error rates.

Performance Metric	Conventional Method	ML-Enhanced Method	Improvement
Detection Limit (ppm)	1.15 ± 0.12	0.50 ± 0.05	2.3× better
False Positive Rate (%)	8.4 ± 0.7	1.1 ± 0.1	87% reduction
Response Time (s)	166 ± 8	98 ± 5	41% faster
Error Rate (%)	12.3 ± 1.1	3.2 ± 0.3	74% reduction
Drift (%/month)	7.8 ± 0.8	2.1 ± 0.2	73% reduction
Cross-sensitivity Ratio	0.31 ± 0.03	0.08 ± 0.01	74% better

4. Conclusion

This comprehensive study demonstrates the successful development and optimization of Ni-doped ZnO gas sensors enhanced through machine learning approaches for NO₂ detection. The incorporation of Ni dopants significantly improved sensor performance, with Zn_{0.90}Ni_{0.10}O exhibiting optimal characteristics including a sensitivity of 11.57 towards 10 ppm NO₂ compared to 2.42 for pure ZnO, shortened response time of 166s, and recovery time of 59s at 200°C. Material characterization revealed systematic changes in structural and optical properties, with band gap reduction from 3.37 eV to 3.16 eV upon Ni doping and decreased crystallite size from 12.6 nm to 11.0 nm.

The integration of machine learning algorithms markedly enhanced sensor capabilities, with SVM classifiers achieving 96.8% accuracy in gas identification and XGBoost regression demonstrating excellent concentration prediction ($R^2 = 0.985$, MAE = 0.15 ppm). The ML-enhanced system showed substantial improvements over conventional methods, including an 87% reduction in false positive rates, a 2.3-fold improvement in detection limit (reaching 0.50 ppm), and 74% reduction in cross-sensitivity. Long-term stability tests confirmed the durability of Ni-doped sensors, with Zn_{0.90}Ni_{0.10}O maintaining 92% of its initial response after 100 measurement cycles. These results establish the synergistic benefits of combining materials engineering with advanced data analytics, offering a promising platform for next-generation gas sensing applications requiring high sensitivity, selectivity, and reliability.

Acknowledgements

Science Foundation of Henan Department of Education (25B416010), Key Scientific and Technological Project of Henan Province (222102320206).

References

- [1] S. Drewniak, Ł. Drewniak, T. Pustelny, *Sensors* 22, 5316 (2022); <https://doi.org/10.3390/s22145316>
- [2] Y. Kang, D. H. Kwak, J. E. Kwon, B.-G. Kim, W. H. Lee, *ACS Applied Materials & Interfaces* 13, 31910 (2021); <https://doi.org/10.1021/acsami.1c05681>
- [3] Z. Yuan, Q. Zhao, Z. Duan, C. Xie, X. Duan, S. Li, Z. Ye, Y. Jiang, H. Tai, *Sensors and Actuators B: Chemical* 363, 131790 (2022); <https://doi.org/10.1016/j.snb.2022.131790>
- [4] X. Yao, J. Zhao, Z. Jin, Z. Jiang, D. Xu, F. Wang, X. Zhang, H. Song, D. Pan, Y. Chen, R. Wei, Z. Guo, J. Liu, N. Naik, R. Wang, L. Wu, *ACS Applied Materials & Interfaces* 13, 26278 (2021); <https://doi.org/10.1021/acsami.1c02176>
- [5] J. N. O. Amu-Darko, S. Hussain, Q. Gong, X. Zhang, Z. Xu, M. Wang, G. Liu, G. Qiao, *Journal of Environmental Chemical Engineering* 11, 109211 (2023); <https://doi.org/10.1016/j.jece.2022.109211>
- [6] J. Li, M. Yang, Y. Li, X. Cheng, X. Zhang, Y. Xu, S. Gao, H. Zhao, L. Huo, *Sensors and Actuators B: Chemical* 361, 131703 (2022); <https://doi.org/10.1016/j.snb.2022.131703>
- [7] Z. Yuan, Q. Zhao, C. Xie, J. Liang, X. Duan, Z. Duan, S. Li, Y. Jiang, H. Tai, *Sensors and Actuators B: Chemical* 355, 131300 (2022); <https://doi.org/10.1016/j.snb.2021.131300>
- [8] S. D. Lokhande, M. B. Awale, G. Umadevi, V. D. Mote, *Materials Chemistry and Physics* 301, 127667 (2023); <https://doi.org/10.1016/j.matchemphys.2023.127667>
- [9] H. Esfandian, M. Rostamnejad Cherati, M. Khatirian, *Inorganic Chemistry Communications* 159, 111750 (2024); <https://doi.org/10.1016/j.inoche.2023.111750>
- [10] Z. Jin, J. Li, Y. Zhang, D. Liu, H. Ding, B. B. Mamba, A. T. Kuvarega, J. Gui, *Journal of Materials Science & Technology* 125, 38 (2022); <https://doi.org/10.1016/j.jmst.2022.01.034>
- [11] M. Y. Ali, M. K. R. Khan, A. M. M. T. Karim, M. M. Rahman, M. Kamruzzaman, *Heliyon* 6, (2020).
- [12] F. Abbasi, F. Zahedi, M. hasan Yousefi, *Optics Communications* 482, 126565 (2021); <https://doi.org/10.1016/j.optcom.2020.126565>
- [13] S. Kanaparthi, S. G. Singh, *Sensors and Actuators B: Chemical* 348, 130725 (2021); <https://doi.org/10.1016/j.snb.2021.130725>
- [14] V. V. Krivetskiy, M. D. Andreev, A. O. Efitorov, A. M. Gaskov, *Sensors and Actuators B: Chemical* 329, 129187 (2021); <https://doi.org/10.1016/j.snb.2020.129187>
- [15] M. Aliramezani, A. Norouzi, C. R. Koch, *Sensors and Actuators B: Chemical* 321, 128414 (2020); <https://doi.org/10.1016/j.snb.2020.128414>
- [16] U. Yaqoob, M. I. Younis, *Sensors* 21, 2877 (2021); <https://doi.org/10.3390/s21082877>
- [17] N. X. Thai, M. Tonezzer, L. Maserà, H. Nguyen, N. V. Duy, N. D. Hoa, *Analytica Chimica Acta* 1124, 85 (2020); <https://doi.org/10.1016/j.aca.2020.05.015>
- [18] I. Ahmad, M. Aslam, U. Jabeen, M. N. Zafar, M. N. K. Malghani, N. Alwadai, F. H. Alshammari, A. S. Almuslem, Z. Ullah, *Inorganica Chimica Acta* 543, 121167 (2022); <https://doi.org/10.1016/j.ica.2022.121167>
- [19] M. Sik Choi, M. Young Kim, A. Mirzaei, H.-S. Kim, S. Kim, S.-H. Baek, D. Won Chun, C. Jin, K. Hyung Lee, *Applied Surface Science* 568, 150910 (2021);

<https://doi.org/10.1016/j.apsusc.2021.150910>

[20] H. Ali, A. M. Alsmadi, B. Salameh, M. Mathai, M. Shatnawi, N. M. A. Hadia, E. M. M. Ibrahim, *Journal of Alloys and Compounds* 816, 152538 (2020);

<https://doi.org/10.1016/j.jallcom.2019.152538>

[21] J. Xu, M. Li, L. Yang, J. Qiu, Q. Chen, X. Zhang, Y. Feng, J. Yao, *Chemical Engineering Journal* 394, 125050 (2020); <https://doi.org/10.1016/j.cej.2020.125050>

[22] I. Elhamdi, H. Souissi, O. Taktak, J. Elghoul, S. Kammoun, E. Dhahri, B. F. O. Costa, *RSC Advances* 12, 13074 (2022); <https://doi.org/10.1039/D2RA00452F>

[23] I. Loyola Poul Raj, A. Jegatha Christy, R. David Prabu, N. Chidhambaram, Mohd. Shkir, S. AlFaify, A. Khan, *Inorganic Chemistry Communications* 119, 108082 (2020);

<https://doi.org/10.1016/j.inoche.2020.108082>

[24] S. Saleem, M. H. Jameel, N. Akhtar, N. Nazir, A. Ali, A. Zaman, A. Rehman, S. Butt, F. Sultana, M. Mushtaq, J. H. Zeng, M. Amami, K. Althubeiti, *Arabian Journal of Chemistry* 15, 103518 (2022); <https://doi.org/10.1016/j.arabjc.2021.103518>

[25] M. Ayachi, F. Ayad, A. Djelloul, L. Benharrat, S. Anas, *Semiconductors* 55, 482 (2021);

<https://doi.org/10.1134/S1063782621050043>

[26] R. Amari, E. Benrezgua, B. Deghfel, Z. Abdelhalim, M. Kamil Yaakob, W. Jeffrey Basirun, A. Boukhari, S. Kheawhom, A. Azmin Mohamad, *Optical Materials* 128, 112398 (2022);

<https://doi.org/10.1016/j.optmat.2022.112398>

[27] Y. Yang, S. Wu, Y. Cao, S. Li, T. Xie, Y. Lin, Z. Li, *Journal of Alloys and Compounds* 920, 165850 (2022); <https://doi.org/10.1016/j.jallcom.2022.165850>